

Ion-Migration Inhibition by the Cation– π Interaction in Perovskite Materials for Efficient and Stable Perovskite Solar Cells

Dong Wei, Fusheng Ma, Rui Wang, Shangyi Dou, Peng Cui, Hao Huang, Jun Ji, Endong Jia, Xiaojie Jia, Sajid Sajid, Ahmed Mourtada Elseman, Lihua Chu, Yingfeng Li, Bing Jiang, Juan Qiao,* Yongbo Yuan, and Meicheng Li*

Migration of ions can lead to photoinduced phase separation, degradation, and current–voltage hysteresis in perovskite solar cells (PSCs), and has become a serious drawback for the organic–inorganic hybrid perovskite materials (OIPs). Here, the inhibition of ion migration is realized by the supramolecular cation– π interaction between aromatic rubrene and organic cations in OIPs. The energy of the cation– π interaction between rubrene and perovskite is found to be as strong as 1.5 eV, which is enough to immobilize the organic cations in OIPs; this will thus lead to the obvious reduction of defects in perovskite films and outstanding stability in devices. By employing the cation-immobilized OIPs to fabricate perovskite solar cells (PSCs), a champion efficiency of 20.86% and certified efficiency of 20.80% with negligible hysteresis are acquired. In addition, the long-term stability of cation-immobilized PSCs is improved definitely (98% of the initial efficiency after 720 h operation), which is assigned to the inhibition of ionic diffusions in cation-immobilized OIPs. This cation– π interaction between cations and the supramolecular π system enhances the stability and the performance of PSCs efficiently and would be a potential universal approach to get the more stable perovskite devices.

3.8 to 22.1% within the past few years.^[1–6] The rocketed improvement of the PSCs is attributed to the easy-crystallized organic–inorganic hybrid perovskite materials (OIPs), which have been demonstrated to be excellent photovoltaic materials, possessing large absorption coefficient, high carrier mobility, long carrier lifetime, and direct bandgap.^[7–9] However, the outstanding perovskite materials also have much intrinsic flaws, such as the migration and loss of organic cations and halide ions during thermal-annealing process and under illumination conditions.^[10–12] The ionic migration problem has been considered as the main reason for the degradation in perovskite films and devices, which cannot be avoided by substituting components of perovskite materials or sealing the devices.^[13–16] In addition, the embarrassing hysteresis in PSCs has been proved to be associated with the ionic migration in perovskite films, which profoundly impacts the practical application of the devices.^[17–20]

Organic–inorganic hybrid perovskite solar cells (PSCs) possess the advantages of low-cost and high performance, especially the impressive strides of power conversion efficiency (PCE) from

In the past few years, ionic migration has attracted wide attention in OIPs including the investigations through both experimental and theoretical methods.^[21–24] It has been

D. Wei, S. Dou, P. Cui, H. Huang, J. Ji, S. Sajid, Dr. A. M. Elseman, Dr. L. Chu, Dr. Y. Li, Dr. B. Jiang, Prof. M. Li
State Key Laboratory of Alternate Electrical Power System with Renewable Energy Sources
School of Renewable Energy
North China Electric Power University
Beijing 102206, China
E-mail: mcli@ncepu.edu.cn
F. Ma, R. Wang, Prof. J. Qiao
Key Lab of Organic Optoelectronics and Molecular Engineering of Ministry of Education
Department of Chemistry
Tsinghua University
Beijing 100084, China
E-mail: qjuan@mail.tsinghua.edu.cn

E. Jia, Dr. X. Jia
Key Laboratory of Solar Thermal Energy and Photovoltaic System
Institute of Electrical Engineering
Chinese Academy of Sciences
Beijing 100190, China
Dr. A. M. Elseman
Electronic and Magnetic Materials Department
Central Metallurgical Research and Development Institute (CMRDI)
PO Box 87 Helwan, 1, Elfelezat Street, El-Tebbin, 11421 Cairo, Egypt
Prof. Y. Yuan
Hunan Key Laboratory of Super-microstructure and Ultrafast Process
School of Physics and Electronics
Central South University
Hunan 410083, P. R. China

 The ORCID identification number(s) for the author(s) of this article can be found under <https://doi.org/10.1002/adma.201707583>.

DOI: 10.1002/adma.201707583

demonstrated that the organic and halide ions in OIPs have low activation energy for migration (0.2–0.8 eV), which make them easy to migrate through the defects and grain boundaries for a long range even at room temperature.^[25,26] These migrated ions leaving lots of vacancies and interstitial ions can form more charge defects in perovskite films.^[27] To suppress the ionic migration, many endeavors had been paid on reducing the pathways of the ionic migration, such as passivation method and grain-growth method to decrease the density of defects and grain boundaries.^[28–30] However, too much works had been paid to constrain the paths of ionic migration instead of inhibiting the ionic migration originally. Indeed, the inhibition of the mobile ions is the key to solve the problem finally in the future, if an effective method could be put forward.

In the OIPs, there are two main mobile ions, that is, organic cations and halide ions, and the organic cations are more sensitive and vulnerable than other ions to the ambient environment.^[31,32] Especially, under illumination, the hydrogen bonding energy between organic cations and Pb–I framework would be weakened and the organic cations in OIPs are proposed to be easier to migrate, which would accelerate the loss of organic cations and the decomposition of OIPs.^[33] By employing an external poling field, the organic cations exhibit obvious redistributions, which could change the chemical and electric equilibrium of OIPs.^[34] Moreover, the migration of organic cations has tremendous impacts on the formation of ionic displacements or charged defects and further speed up the ionic migration.^[17,35] Hence, it is more imperative to immobilize the organic cations to improve stability and optoelectronic properties of OIPs.

Herein, inspiration from ubiquitous cation– π interactions in many supramolecular systems, such as biology and medicine,^[36,37] for the first time, we introduce a new-type chelation-like cation– π interaction into OIPs by mixing aromatic rubrene into perovskite films during film-forming process to restrict the organic cations from migration (as shown in Figure S1, Supporting Information). The unique cation– π interaction between rubrene and perovskite brings astonishing stabilization with the calculated interaction energy about 1.5 eV, which is strong enough to immobilize the organic cations with low activation energy (e.g., 0.5–0.8 eV for MA⁺ ions), thus helping acquire defectless and stable perovskite films. By employing these cation-immobilized perovskite films, PSCs display superior performance in stability and efficiency. The PCE of PSCs with rubrene exhibits significant increase from 18.60 to 20.86%. Meanwhile, the stability of PSCs with rubrene has been enhanced dramatically, which maintains 98% of the initial efficiency after 30 d even under the relative humidity at 70%. In addition, with the inhibition of ionic migration, the hysteresis of PSCs with rubrene is also suppressed greatly compared with the standard PSCs.

Essentially, cation– π interaction is a kind of noncovalent forces between the face of an electron-rich π system and an adjacent cation, which is proposed to occur between aromatic π moieties and the organic cations in OIPs. To clarify the properties of cation– π interaction between rubrene and perovskite materials, the interaction energies of MA⁺ cations–rubrene have been calculated by density functional theory (Gaussian 09 software). Considering the condition that MA⁺ cations could

interact with different π moieties of rubrene, four possible initial geometries were optimized under B3LYP-D3/6-311++G(d,p) level with dispersion corrections,^[38] followed by single-point energy calculations for correction of basis set superposition error (BSSE). As shown in Figure 1a, the optimized geometry with the largest interaction energy demonstrates a chelation-like interaction between MA⁺ cations and rubrene. Specifically, for MA⁺ cations, two N–H bonds toward rubrene hook the central tetracene and the pending phenyl group through $\sigma_{\text{N–H}}^*-\pi_{\text{rubrene}}$ interactions, respectively.^[39,40] Accordingly, their bond lengths (1.04 Å) are a little longer than that of the other N–H bond pointing away from rubrene (1.02 Å). To further visualize this special interaction, electrostatic potential is mapped on the molecular surface where electron density is 0.012 au. As shown in Figure 1b, MA⁺ cations covered with positive charge would draw the nearing polarizable π electrons from rubrene and result in a continuous electron distribution at the junction of MA⁺–rubrene.^[41,42] Most notably, the interaction energy of MA⁺–rubrene is calculated to be –35.4 kcal mol^{–1} (–1.53 eV), which is almost twice higher than that of a common cation– π interaction system like MA⁺–benzene (–18.8 kcal mol^{–1}, in gas phase). Such strong interaction is proposed to be originated from the synergetic effect of multiple off-axis cation– π interactions.^[41] Therefore, the mobile MA⁺ cations could be anchored firmly by rubrene. Other optimized geometries are listed in Figure S2 and Table S1 (Supporting Information), which also show chelation-like interactions and large interaction energies of over –30 kcal mol^{–1} (1.30 eV) between MA⁺ and rubrene. In addition, the calculations on FA⁺ and rubrene system suggest that FA⁺ cations and rubrene would also interact with each other through the cation– π interaction (Figure S3, Supporting Information). According to the results of calculation, the cation– π interaction between rubrene and perovskite is strong enough to immobilize the MA⁺/FA⁺ cations at the surfaces and grain boundaries as shown in Figure 1c.

To certify the interaction between rubrene and perovskite, the Fourier transform infrared (FTIR) spectra measurement was employed for the perovskite film with rubrene in comparison with pristine perovskite film and rubrene film. As shown in Figure 1d, the FTIR spectrum of pristine perovskite film contains peaks at 908 cm^{–1} (CH₃–NH₃⁺ rocking), 1350 cm^{–1} (C–H stretch), 1465 cm^{–1} (N–H bending), 1714 cm^{–1} (N–H bending), and 3132 cm^{–1} (N–H stretch), which are all assigned to the bending and stretching modes of C–H and N–H modes within the organic group of perovskite.^[43] For the FTIR spectrum of rubrene, there are several obvious peaks belonging to the C–C and C=C bending modes of rubrene. However, when it came to perovskite film with rubrene, all these characteristic peaks associated with the C–H, N–H, C–C, and C=C bond from the pristine perovskite and rubrene are enormously diminished. It indicates that the introduced rubrene can restrict the motion of organic group in perovskite through the supramolecular cation– π interaction, which also confirms the results of DFT calculation.

To verify the effects of cation– π interaction on suppressing the migration of organic groups in perovskite devices, a special device with the structure indium tin oxide (ITO)/SnO₂/perovskite (with and without rubrene)/PbI₂/Au had been designed and fabricated. In this special structure, the

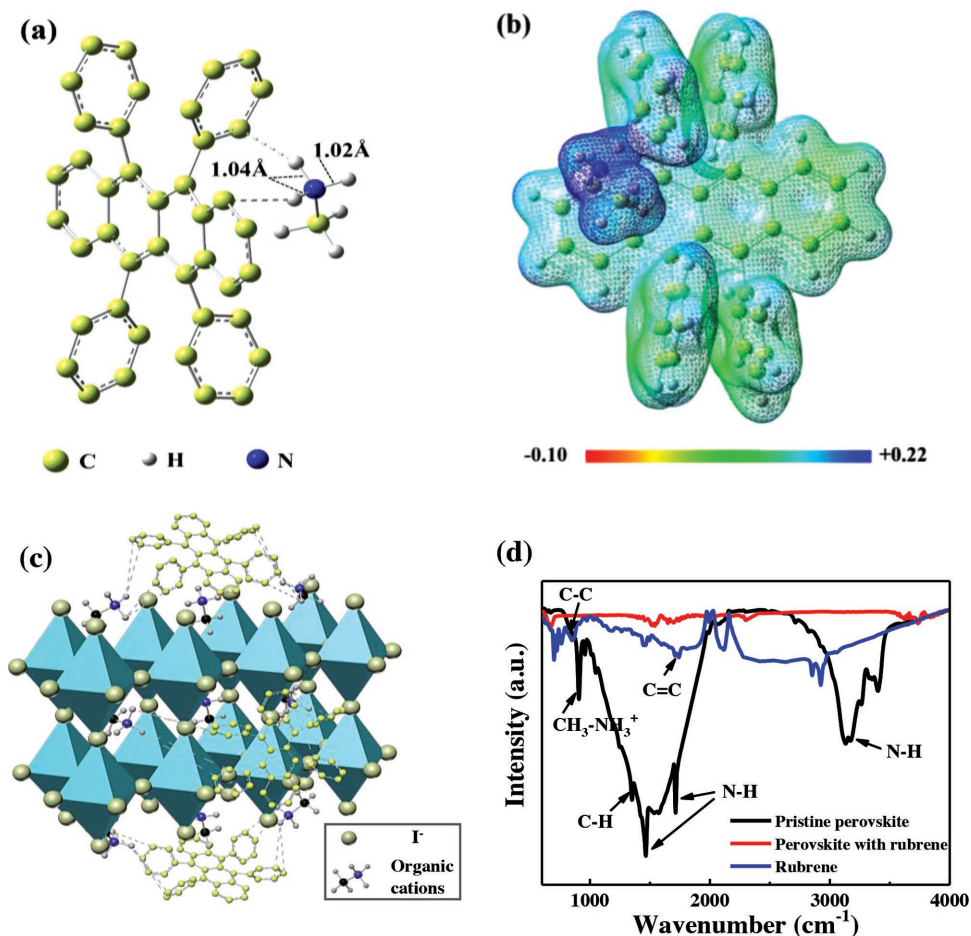


Figure 1. Mechanisms of cation- π interaction between perovskite and rubrene in perovskite films. a) DFT calculations for the optimized configurations of MA⁺-rubrene with the largest interaction energy ($-35.4 \text{ kcal mol}^{-1}$). Hydrogen atoms of rubrene are omitted for the sake of clarity. b) Corresponding electrostatic potential mesh maps of MA⁺-rubrene, isovalue = 0.012. c) Schematic illustration of the cation- π interaction between rubrene and organic cations of perovskite. d) FTIR spectra of perovskite films with and without rubrene layer and the rubrene film in the range of 600–4000 cm^{-1} . All of these films were fabricated on ITO substrate.

migration of organic groups to the pristine PbI_2 layer will cause the irreversible formation of perovskite, which can then be traced by time-of-flight secondary ion mass spectroscopy (TOF-SIMS) measurement. Therefore, the ion migration influenced by rubrene can be directly investigated. In order to accumulate the migration of cations, we employed a DC bias (1 V) with Keithley 2400 source meter on the as-prepared devices for 72 h under the continuous illumination of Xe lamp at 90 °C in ambient air. It is expected that the organic groups of perovskite would migrate from the perovskite layer to the PbI_2 layer obviously under this tough condition, if these are not restricted in the perovskite layer.

Here, the TOF-SIMS was employed to explore the organic groups whether they had migrated from the perovskite layer to the PbI_2 layer after the consecutive operation for 72 h. For the device fabricated by the perovskite film without rubrene, as shown in Figure 2a, it is obvious that the CN^- ions remarkably diffused into the PbI_2 layer from the pristine perovskite layer, which indicates the serious migration of organic cations. In contrast, for the device fabricated by the perovskite film with rubrene, the diffusion of CN^- ions into PbI_2 layer is negligible

as shown in Figure 2b. In addition, the intensity of CN^- ions in the perovskite with rubrene is much stronger than that in the pristine perovskite after the same operating process. This demonstrates that the cation- π interaction between rubrene and perovskite is critical and effective for suppressing the migration of organic cations in perovskite. In addition, to further investigate the effect of cation- π interaction on the inhibition of ionic migration at high temperature, the perovskite films with and without rubrene had been annealed at 90 °C for 10 h as shown in Figure S4 (Supporting Information). X-ray diffraction (XRD) had been employed to measure the compositional changes of these films as shown in Figure S5 (Supporting Information). The insets are the digital photos of the measured films after a long-term annealing operation. By comparisons of XRD patterns and photos from these films, it is obvious that the perovskite film with rubrene exhibited better stable property than that of the perovskite film without rubrene. This indicates that the cation- π interaction between rubrene and perovskite can suppress the migration of ions efficiently even at relatively high temperature, which confirm with the abovementioned results of DFT calculation and TOF-SIMS.

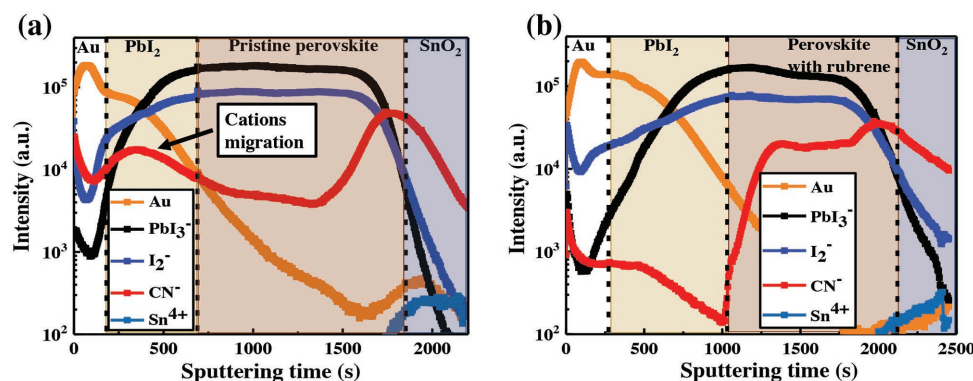


Figure 2. Effect of cation- π interaction for suppressing the migration of organic cations in perovskite devices. TOF-SIMS elemental depth profiles of Au, PbI_3^- , CN^- , and Sn^{4+} of the devices a) without rubrene and b) with rubrene. The devices were designed and structured as ITO/ SnO_2 /perovskite (with and without rubrene)/ PbI_2 /Au. All of these devices for the TOF-SIMS measurement were operated for 72 h with 1 V DC bias under the continuous illumination of Xe lamp at 90 °C in ambient air.

Owing to the cation- π interaction between rubrene and perovskite suppressing the migration of organic cations in perovskite films, it can be deduced that this interaction would play a role of inhibiting the formation of defects involved with the migration of cations. To investigate the effects of rubrene on the surficial properties of perovskite films, X-ray photoelectron spectroscopy (XPS) was employed for the films with and without rubrene, and the spectra of Pb 4f of these films are

shown in Figure 3a. The survey spectra of perovskite films with and without rubrene are also exhibited in Figure S6 (Supporting Information). As shown in Figure 3a, Pb 4f core level of pristine perovskite film includes two main peaks centered on 138.3 and 143.2 eV, which are assigned to lead iodine component in perovskite.^[44] Meanwhile, two additional weak peaks located on 136.8 and 141.8 eV are associated to metallic Pb, which is caused by the decomposition of perovskite.^[45] In contrast, the

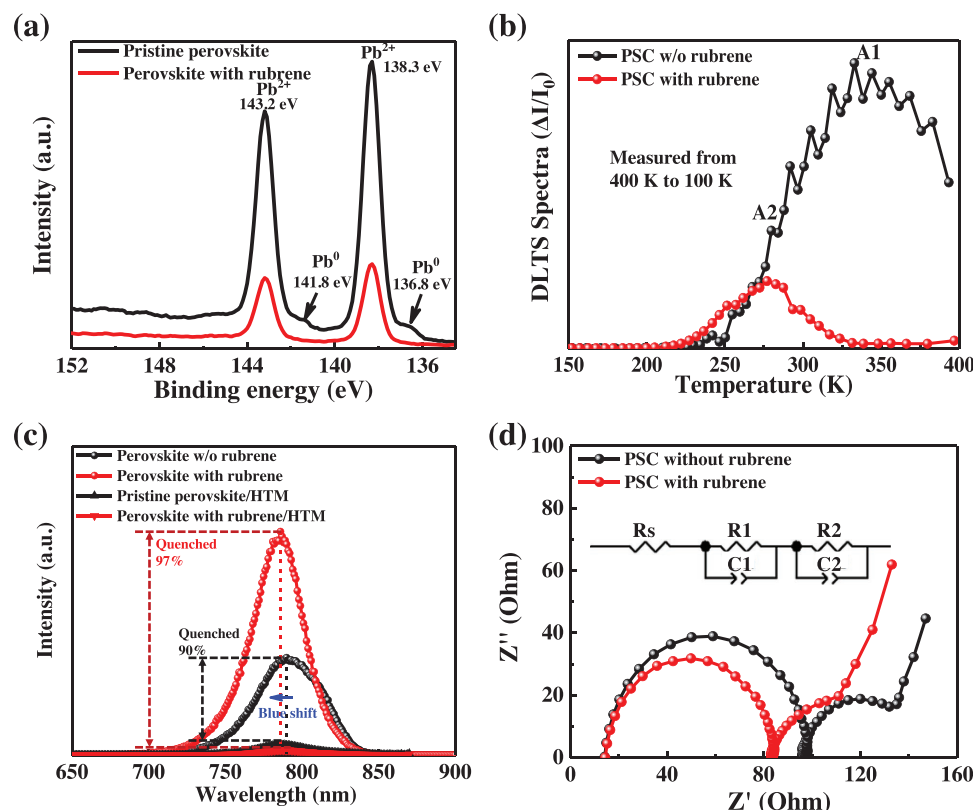


Figure 3. Influences of cation- π interaction on the formation of defects in perovskite films and the charge transport properties in devices. a) The spectra of Pb 4f obtained from pristine perovskite films and perovskite with rubrene. b) DLTS spectra of the PSC without and with rubrene measured between 400 and 100 K. c) PL spectra of perovskite films with and without rubrene and the as-prepared films with HTM layer. d) Nyquist plots of PSCs with and without rubrene. The inset is the equivalent circuit model for fitting curves.

weak peaks corresponding to metallic Pb disappeared in the cation-immobilized perovskite film with rubrene, which indicates that the supramolecular cation- π interaction can repress the formation of metallic Pb in OIPs and prevent the perovskite film from decomposition during the thermal-annealing process for fabricating perovskite films.

To obtain further insight into the influence of the supramolecular cation- π interaction on the formation of these defects, the deep-level transient spectroscopy (DLTS) was performed as shown in Figure 3b. These peaks arise because of the emission rate from a trap responding at a given frequency, which depends very strongly on the energy of the trap and the measured temperature. As shown in Figure 3a, there arise two peaks denoted A1 and A2 for the pristine perovskite film with the temperature scan, indicating two dominant deep-level defects in the pristine perovskite film. In comparison, for the perovskite film with rubrene, the A1 peak disappears completely and the A2 peak decreases over 50% compared with the pristine perovskite film. This indicates that the defects located in the A1 level can be healed perfectly by the presence of rubrene. According to the Arrhenius equation:

$$e_n = N_c \langle v_{th} \rangle \sigma_n \exp\left(\frac{-E_T}{kT}\right) \quad (1)$$

The trap activation energy represented by E_T in Equation (1) can be obtained by fitting the slopes of the plot of $\ln(\sigma_n \langle v_{th} \rangle N_c)$ versus $1/kT$. As shown in Figure S7 (Supporting Information), the trap activation energy of A1 and A2 peaks in pristine perovskite film are calculated to be 0.39 and 0.26 eV, respectively. The relatively deep-level defects related with A1 peak are assumed to be the defects associated with organic cations, such as the vacancy defects of FA^+ and MA^+ cations.^[16,46] The defects related with A2 are considered to be the interstitial defects originating from interstitial iodide and lead.^[47,48] According to the analysis of DLTS, all of these defects are efficiently suppressed by means of the strong supramolecular cation- π interaction between the organic cations and rubrene. This demonstrates that the cation- π interaction between rubrene and perovskite can inhibit the formation of defects during the fabricating process of perovskite films and can passivate the charged defects effectively in perovskite films.

As the cation-immobilized perovskite films have fewer defects, the nonradiative recombination process related with defects would be inhibited and the transfer of carriers in perovskite films would be more efficient. Meanwhile, as the highest occupied molecular orbital level (-5.4 eV) of rubrene is similar to the valence band of the perovskite,^[49] the hole transfer from perovskite to rubrene may occur, whereas the nonradiative energy transfer from perovskite to rubrene is less possibly to occur due to the much larger bandgap of rubrene than that of the perovskite. Here, the photoluminescence (PL) spectra of perovskite films with and without rubrene were performed in comparison with those of these films with HTM layer (Spiro-OMeTAD layer). As shown in Figure 3c, the perovskite film with rubrene demonstrates much stronger and a slight blueshifted emission than that of the pristine perovskite film. This can be attributed to the reduced recombination processes in the perovskite films with rubrene,^[50,51] which is consistent with the

abovementioned results. The PL spectra of perovskite films with various concentrations of rubrene were also obtained and shown in Figure S8 (Supporting Information), which presents the same trend. In addition, the HTM layer was introduced on the surface of perovskite films with and without rubrene to detect the charge extraction and transfer between perovskite films and HTM layers. As shown in Figure 3c, the PL of the sample of pristine perovskite/HTM quenches about 90% in comparison with that without HTM, while the PL of the sample of perovskite with rubrene/HTM quenches more than 97% in comparison with that without HTM. The larger quenched PL demonstrates that the perovskite film with rubrene possesses much higher charge-extraction and transfer efficiency in complete devices, which is consistent with other previous works.^[52,53] Hence, the presence of cation- π interaction in the perovskite films could minimize the charge losses induced by the trap states and enhance the efficiency of charge transport as well.

It has been proved that the ionic migration can affect the electrostatics of the device quite significantly and could lead to a reduction in collection efficiency.^[54] Accordingly, the Nyquist plot of the electrochemical impedance spectra (EIS) was employed to further understand the properties of charge transport in perovskite devices with and without rubrene as shown in Figure 3d. These devices were measured under the illumination of AM 1.5G in ambient air, and the spectra were obtained for 1.0 V DC bias in a frequency range of 0.2–200 kHz. The inset in Figure 3d is the equivalent circuit model employed to fit the spectra. In the equivalent circuit model, R1 associated with the higher frequency arc is attributed to impedance arising from the selective contact and charge transport at the interface between perovskite and selective layers; C1 is the chemical capacitance of the film. R2 and C2 associated with the lower frequency arc are attributed to HTM resistance, capacitance, and the extraction in the Au electrode.^[55,56] From the values fitted by the equivalent circuit model, R1 changes from 78.62 Ω (obtained from the pristine perovskite film) to 65.86 Ω (obtained from the perovskite film with rubrene). The decrease of R1 indicates the enhancement of charge transport efficiency in devices. This can be attributed to the introduction of rubrene in the perovskite film, which suppresses the migration of cations and inhibits the formation of defects.

Considering the outstanding effects of cation- π interaction between rubrene and OIPs as exhibited above, the performance and stability of PSCs fabricated by the cation-immobilized OIPs (labeled as PSCs with rubrene) are expected to present better than the standard planar PSCs. To demonstrate its potential, we fabricated the $FA_{0.15}MA_{0.85}PbI_3$ -based PSCs with various concentrations of rubrene. The surface morphology and the XRD pattern of the $FA_{0.15}MA_{0.85}PbI_3$ -based perovskite films with and without rubrene are exhibited in Figure S9 (Supporting Information). From scanning electron microscopy (SEM) figures, the morphology of the pristine perovskite film is compact and smooth with the average grain size of ≈ 300 nm shown in Figure S9a (Supporting Information). For the perovskite film with rubrene shown in Figure S9b (Supporting Information), it is obvious that the surface of the perovskite film has been covered by a thin layer formed by large number of particles. These coating particles are supposed to be rubrene grains as

shown in Figure S9c (Supporting Information). XRD was also employed to investigate the crystallinity of the perovskite films with and without rubrene as shown in Figure S9d (Supporting Information). In the pristine perovskite film, an additional diffraction peak located at 12.6° can be observed, which indexes to the (001) plane of PbI_2 , demonstrating that the fresh pristine perovskite film is stoichiometric with less organic groups after thermal-annealing process.^[57] For the perovskite film with rubrene, it is clear that these diffraction peaks are indexed to the perovskite without any other undesired peaks. The crystallinity of the perovskite films with and without rubrene is similar according to the values of full width at half maximum (FWHM) as shown in Table S2 (Supporting Information). The slightly increased FWHM of the XRD peaks may be caused by rubrene molecules remaining in perovskite crystals. The current-density–voltage (J - V) curves of the $\text{FA}_{0.15}\text{MA}_{0.85}\text{PbI}_3$ -based PSCs with various concentrations of rubrene are shown in Figure S10 (Supporting Information). The average results of photovoltaic parameters obtained from 20 PSCs including short-circuit current density (J_{SC}), open-circuit voltage (V_{OC}), fill factor (FF), and photoelectric conversion efficiency (PCE) are summarized in Table S3 (Supporting Information). It can be seen that the performance of the PSCs prepared from different concentration of rubrene presents an increase–decrease trend in device performance, especially in J_{SC} , FF, and PCE, indicating that the presence of rubrene in perovskite, despite its trace amount, has remarkable influence on the performance of PSCs. As shown in Figure 4a, the PSCs with 10 mg mL^{-1} concentration of rubrene in chlorobenzene exhibit the champion PCE of 20.86%, 12% higher than that of the standard planar

PSCs without rubrene (18.60%). Strikingly, the improvement of J_{SC} is the largest from 22.26 to 24.20 mA cm^{-2} among different parameters of the performance of devices. The steady-state photocurrent and efficiency of PSC with rubrene measured over a period of 200 s at the maximum power point are presented in Figure 4b. By holding a bias near the maximum power output point (0.95 V), we obtained a stabilized PSC of $\approx 20.63\%$, very close to the highest PCE of 20.86% for the same cell. In addition, to certify the veracity of these results yield in our lab, an optimized PSC with rubrene was sent to the National Institute of Metrology of China (NIM) for certification, and a PCE of 20.80% was obtained as shown in Figure S11 (Supporting Information).

To find out the intrinsic reason for the increase of J_{SC} from the PSCs with rubrene, the external quantum efficiencies (EQE) of PSCs with and without rubrene have been characterized. In Figure 4c, it is clear that the EQE of PSC with rubrene is higher than the standard PSC over the entire wavelength measurement range. The integrated J_{SC} from EQE curves also agree with the measured J_{SC} very well. Furthermore, the EQE of PSCs with and without rubrene was also calculated as shown in Figure S12 (Supporting Information). The EQE of the PSC with rubrene is almost 100% meaning that the PSC with rubrene possesses less recombination centers and higher efficiency of transport of photogenerated carriers.^[58,59] Hence, such notable increase of J_{SC} of the PSC with rubrene could be mainly attributed to the decrease of defects and the high efficiency of charge transport in the cation-immobilized perovskite films, which can further suppress the loss of photoinduced carriers during transfer and enhance the collection of photoinduced carriers in

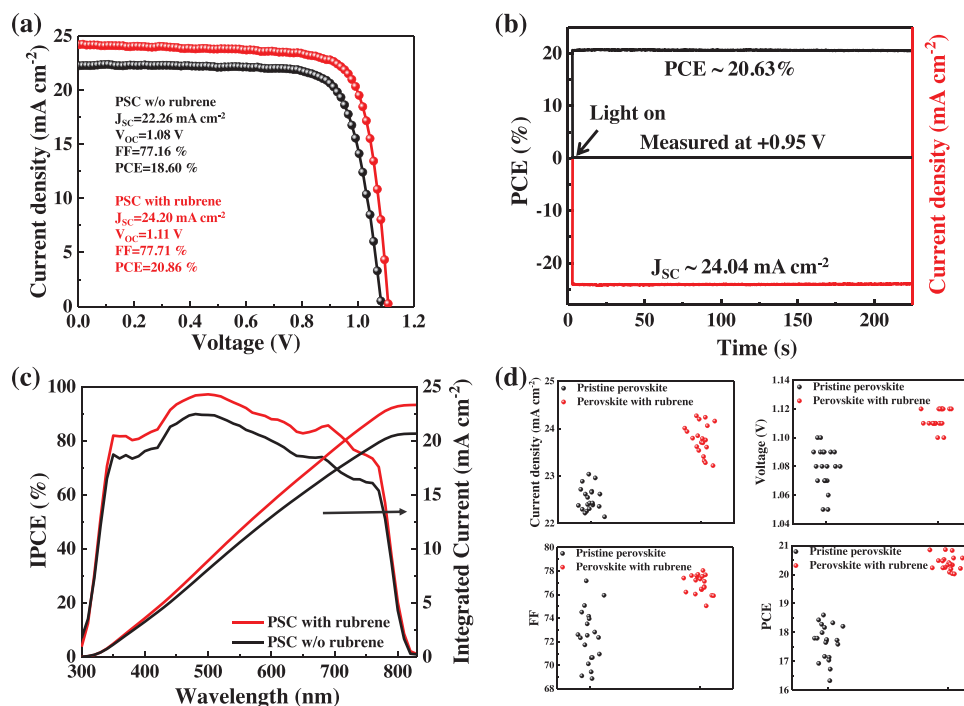


Figure 4. Photovoltaic performance of the PSCs with and without rubrene. a) J - V curves (reverse scan) of the champion PSCs with and without rubrene. b) Steady-state photocurrent and efficiency at the maximum power point (0.95 V) of PSCs with rubrene. c) IPCE curves and the corresponding integrated current of PSCs. d) Photovoltaic metrics of PSCs. All the PSCs were nonencapsulated and measured at the AM 1.5G illumination in ambient air.

PSCs. And the advantages on transfer and collection of carriers possessed by the PSCs with rubrene are considered as the main reasons for obvious improvements in V_{OC} and FF of PSCs.

Meanwhile, the reproducibility of PSCs with rubrene was also investigated. As shown in Figure 4d, it is clear that the perovskite films with rubrene greatly improve the performance and reproducibility of PSCs compared to the standard PSCs. The PCEs for 20 standard PSCs were widely distributed from 16.33 to 18.60%, with average J_{sc} of 22.52 mA cm^{-2} , V_{oc} of 1.08 V, and FF of 72.42%. In comparison, for the PSCs with rubrene, the PCEs were distributed in a narrow range between 20.02 and 20.86%. The average PCE reaches up to 20.39% with an average J_{sc} of 23.80 mA cm^{-2} , V_{oc} of 1.11 V, and FF of 76.90%.

Moreover, the hysteresis of PSCs with rubrene is also improved compared with the standard PSCs as shown in Figure S13 (Supporting Information). The low hysteresis of the

PSCs with rubrene could be originated to the supramolecular cation- π interaction between perovskite and rubrene, which reduces the concentration of defects, hinder the motion of organic ions, and enhances the interfacial charge transfer process as evidenced above.

Besides the high efficiency, long-term stability is the other critical characteristic for PSCs, especially the operational stability in ambient air. To study the stability of PSCs with and without rubrene, the as-prepared PSCs (without encapsulation) had been measured every 3 d for one month under AM1.5 illumination condition. In the measurement intervals, these measured PSCs were stored in a glass oven keeping the humidity at 70% and the temperature at 25 °C. As shown in Figure 5a, the PSCs with rubrene exhibited an excellent long-term stability compared with the standard PSCs. After the continuous operational measurement for one month, the PCE

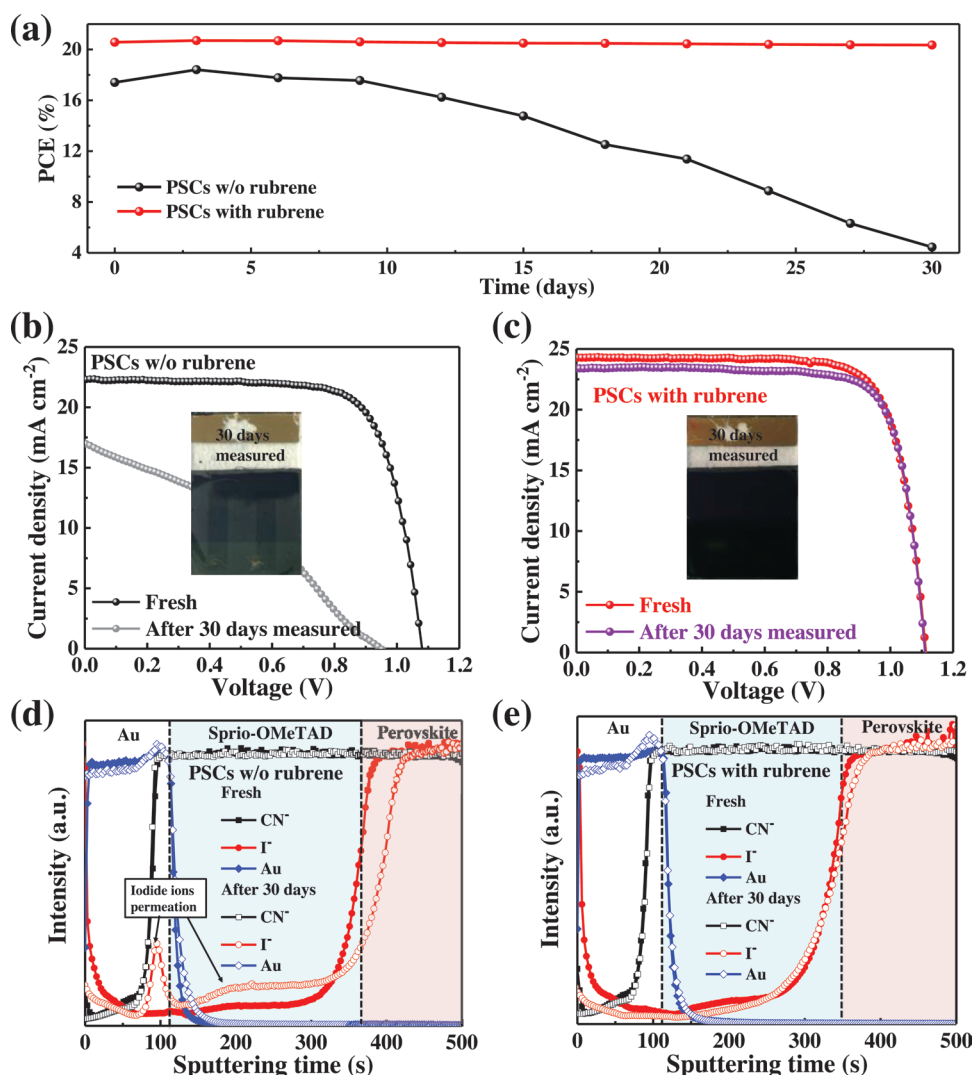


Figure 5. Stability of the perovskite films and devices with and without rubrene. a) Long-term stability of PSCs for one month. These PSCs were measured every 3 d and stored in ambient air before and after J - V measurement. b) J - V curves of PSC without rubrene as freshly prepared and after 30 d operation. c) J - V curves of PSC with rubrene as freshly prepared and after 30 d operation. Inset photos are PSCs after 30 d operation. These photos were obtained from the glass side under the illumination of simulated sunlight equipment. d,e) TOF-SIMS elemental depth profiles of CN^- , I^- , and Au of devices without rubrene (d) and with rubrene (e) as freshly prepared and after 30 d operation.

of PSCs with rubrene changes slightly from 20.57 to 20.35%, maintaining 98% of the initial efficiency. In contrast, the PCE of the standard PSCs decreased severely from 17.41 to 4.45%, which indicates that the standard planar PSCs without rubrene present poor stability and rapid degradation in this testing condition. The J - V curves of PSCs with and without rubrene as freshly prepared and after 30 d operation are exhibited in Figure 5b,c, respectively. The digital photos of these devices after 30 d operation are also presented as inset in Figure 5b,c, which were obtained from the ITO glass side under the AM 1.5G illumination. After 30 d operation, the device without rubrene exhibits a heavy shade of gray in the photoactive area, and the Au electrodes can be seen clearly through the whole devices. In contrast, the photo of device with rubrene presents a dark-brown color, which indicates that the active layers, especially perovskite films of PSCs with rubrene are still intact after a long-term operation. Furthermore, the aging operation of tracking the maximum power point of the PSCs with and without rubrene was also performed as shown in Figure S14 (Supporting Information). All the PSCs were measured by tracking the maximum power point of 0.95 V at the room temperature (≈ 23 °C) under the AM 1.5G illumination of Xe lamp without any filter in ambient air. In Figure S14a (Supporting Information), it is obvious that the PSCs with rubrene exhibit more stable performance than the PSCs without rubrene after a continuous illumination for 5000 s. The PSCs with rubrene maintain 85% of the initial efficiency, in contrast, the efficiency of solar cells without rubrene has almost been degraded totally. Subsequently, we measured the J - V curves of these operated PSCs under the same conditions after stored in dark for 2 h. As shown in Figure S14b (Supporting Information), the performance of the PSCs with rubrene is largely recovered from the degrading state compared with the PSCs without rubrene. These results indicate that the PSCs with rubrene have better long-term stability than the PSCs without rubrene. This can be attributed to the supramolecular cation- π interaction between rubrene and perovskite, which could suppress the migration of organic groups in PSCs under working conditions and inhibit the formation of defects at the surfaces and grain boundaries in perovskite films.

To explore the origin of degradation during the long-term operation, TOF-SIMS was performed for detecting the changes of elements and molecular information in PSCs before and after 30 d operation. The depth profiles obtained from TOF-SIMS (Figure S15, Supporting Information) directly provide the elemental distribution information through the devices. The depth profiles of CN^- , I^- , and Au of PSCs functioned with the sputtering time from 0 to 500 s are shown in Figure 5d,e. For the PSC without rubrene (Figure 5d), I^- ions remarkably diffused into the Spiro-OMeTAD layer and the Au electrode after a long-term operation, whereas the diffusion of I^- ions is negligible for PSC with rubrene (Figure 5e). This is because that the perovskite films with rubrene possess less defects at the surfaces and grain boundaries which are considered as the dominate channels for migration of ions.^[24] For the pristine perovskite, the migrated partial organic species away from the surfaces and grain boundaries could leave relatively open spaces for ion migration. However, for the perovskite with rubrene, the strong cation- π interaction between rubrene

and organic cations could avoid the unintended migration of organic species and suppress the formation of defects, thus effectively shield against the diffusions of ions between different layers in PSCs and enabling PSCs with high efficiency and long-term stability.

In summary, the cation- π interaction was first introduced into perovskite materials, which is effective for suppressing the migration of organic cations in OIPs, thus enabling the cation-immobilized perovskite films with less density of defects and more stable crystal frameworks. By employing the cation-immobilized perovskite films, the high-efficient PSCs with the best efficiency of 20.86% have been achieved, with negligible photocurrent hysteresis. In addition, the cation-immobilized perovskite films successfully inhibit the diffusion of iodine ions between different layers in PSCs under long-term operation, and thus protect the interfaces of transfer layers from diffusion-caused damage. As a result, the PSCs with rubrene maintained 98% of the initial efficiency after 720 h operation. This work provides an efficient approach to acquire the defectless and crystal framework-stable OIPs by introducing the cation- π interaction into perovskite materials. It could be expected that the cation- π interaction can be broadly applied to other high-stable optoelectronic applications as well, such as light-emitting diodes, photodetectors, and lasers.

Experimental Section

Materials: Methylammonium iodide, formamidineum iodide, and 2,20,7,70-tetrakis [N,N-di(4-methoxyphenyl)amino]-9,90-spirobifluorene were purchased from Xi'an Polymer Light Technology Corp. (Purity: 99.5%). Lead iodide, rubrene, and SnO_2 colloid precursor were purchased from Alfa Aesar. N,N-Dimethylformamide (DMF), dimethyl sulfoxide (DMSO), and chlorobenzene were purchased from Acros Organics (Extra dry).

Solution Preparation: SnO_2 solution was prepared according to the report of Jiang et al.^[60] 1 mL of SnO_2 colloid precursor was diluted by 5 mL of deionized water. To prepare the perovskite precursor solution, 0.15 M of FAI, 0.85 M of MAI, and 1.025 M of PbI_2 were mixed in anhydrous dimethylformamide/dimethylsulfoxide (600 mg/78 mg) solution, which was stirred for 2 h at room temperature in the glove box. To prepare the various concentrations of rubrene/chlorobenzene solution (0–20 mg mL⁻¹), different weights of rubrene were dissolved in chlorobenzene, and the rubrene/chlorobenzene solution was stirred for 1 h in the glove box. To prepare the HTM precursor, Spiro-OMeTAD was solved in chlorobenzene with the concentration of 80 mg mL⁻¹ and then *tert*-butylpyridine (28.5 μ L in 1 mL chlorobenzene), and lithium bis-(trifluoromethanesulfonyl) imide (8.75 mg mL⁻¹) were added into the Spiro-OMeTAD solution as the additives, which was stirred in the glove box for 6 h as previous works.^[61,62]

Perovskite Solar Cell Fabrication and Characterization: ITO glass (10 Ω sq⁻¹) was cleaned by sequential sonication with a detergent solution, deionized water, acetone, and isopropyl alcohol for 20 min, respectively. After dried by a nitrogen flow, the substrates were treated with UV-ozone for 15 min before use. SnO_2 films were fabricated by spin-coating the precursor solution onto the ITO substrates at 3000 rpm for 30 s, followed by annealing at 150 °C for 30 min in air. After cooled down to the room temperature, SnO_2 films were further treated with UV-ozone for 15 min and then transferred into the N_2 -filled glove box. To fabricate perovskite films, the perovskite precursor was spin-coated directly on the SnO_2 substrate at 4000 rpm for 30 s. During the spin-coating step, 0.5 mL solution of chlorobenzene with various concentrations of rubrene was poured on the surface at 15 s before the end. The light-yellow transparent films were converted into the

brownish-red perovskite films by heating at 130 °C for 15 min. Then the Spiro-OMeTAD solution was spin-coated at 4000 rpm for 30 s on the perovskite films. Finally, 80 nm Au electrode was evaporated on the films.

Current–voltage curves were measured using a source meter (Keithley 2400) under AM 1.5G irradiation with a power density of 100 mW cm⁻² from a solar simulator (XES-301S+EL-100) by forward (–0.1 to 1.2 V) or reverse (1.2 to –0.1 V) scans. The step voltage was fixed at 12 mV and the delay time was set at 10 ms. The valence spectra were measured by XPS (ESCSLAB 250Xi). All spectra were shifted to account for sample charging using inorganic carbon at 284.80 eV as a reference. The steady PL spectra of the perovskite films on ITO substrates were measured by a spectrometer (Edinburg PLS 980). The EQE was measured using QE-R systems (Enli Tech.). TOF-SIMS measurements (Model TOF-SIMS 5, ION-TOF GmbH) were performed with the pulsed primary ions from a Cs⁺ (2 keV) liquid-metal ion gun for the sputtering and a Bi⁺ pulsed primary ion beam for the analysis (30 keV). FTIR spectroscopy was measured by Horiba Bruker (Germany) from 600 to 4000 cm⁻¹.

Supporting Information

Supporting Information is available from the Wiley Online Library or from the author.

Acknowledgements

D.W. and F.M. contributed equally to this work. This work was partially supported by National Natural Science Foundation of China (Grant Nos. 51772096, 51372082, 51402106, and 11504107), Beijing Natural Science Foundation (17L20075), Joint Funds of the Equipment Pre-Research and Ministry of Education (6141A020225), National Key R&D Program of China (No. 2016YFB0401003), National High-tech R&D Program of China (863 Program, No. 2015AA034601), Par-Eu Scholars Program, Beijing Municipal Science and Technology Project (Z161100002616039), and the Fundamental Research Funds for the Central Universities (2016JQ01, 2017ZZD02).

Conflict of Interest

The authors declare no conflict of interest.

Keywords

cation– π interaction, DFT calculations, efficient and stable perovskite solar cells, ion migration inhibition, perovskite materials

Received: December 28, 2017

Revised: April 20, 2018

Published online:

- [1] A. Kojima, K. Teshima, Y. Shirai, T. Miyasaka, *J. Am. Chem. Soc.* **2009**, *131*, 6050.
- [2] W. Yang, J. Noh, N. J. Jeon, Y. C. Kim, S. Ryu, J. Seo, S. H. Im, *Science* **2015**, *348*, 1234.
- [3] X. Li, D. Bi, C. Yi, J. D. Décoppet, J. Luo, S. M. Zakeeruddin, A. Hagfeldt, M. Grätzel, *Science* **2016**, *353*, 58.
- [4] M. Saliba, T. Matsui, K. Domanski, J. Y. Seo, A. Ummadisingu, S. M. Zakeeruddin, J. P. Correa-Baena, W. Tress, A. Abate, A. Hagfeldt, M. Grätzel, *Science* **2016**, *354*, 206.
- [5] K. T. Cho, S. Paek, G. Grancini, C. R. Carmona, P. Gao, Y. Lee, M. K. Nazeeruddin, *Energy Environ. Sci.* **2017**, *10*, 621.
- [6] W. S. Yang, B. W. Park, E. H. Jung, N. J. Jeon, Y. C. Kim, D. U. Lee, S. S. Shin, J. Seo, E. K. Kim, J. H. Noh, S. Seok, *Science* **2017**, *356*, 1376.
- [7] N. G. Park, *CrystEngComm* **2016**, *18*, 5977.
- [8] Y. Rong, L. Liu, A. Mei, X. Li, H. Han, *Adv. Energy Mater.* **2015**, *5*, 1501066.
- [9] Q. Dong, Y. Fang, Y. Shao, P. Mulligan, J. Qiu, L. Cao, J. Huang, *Science* **2015**, *347*, 967.
- [10] Y. Yuan, Q. Wang, Y. Shao, H. Lu, T. Li, A. Gruverman, J. Huang, *Adv. Energy Mater.* **2015**, *6*, 1501803.
- [11] T. Y. Yang, G. Gregori, N. Pellet, M. Graetzel, J. Maier, *Angew. Chem., Int. Ed.* **2015**, *54*, 7905.
- [12] R. A. Belisle, W. H. Nguyen, A. R. Bowring, P. Calado, X. Li, S. J. C. Irvine, M. D. McGehee, P. R. F. Barnes, B. C. O'Regan, *Energy Environ. Sci.* **2017**, *10*, 192.
- [13] M. L. Agiorgousis, Y. Y. Sun, H. Zeng, S. Zhang, *J. Am. Chem. Soc.* **2014**, *136*, 14570.
- [14] Y. Lin, L. Shen, J. Dai, Y. Deng, Y. Wu, Y. Bai, X. Zheng, J. Wang, Y. Fang, H. Wei, W. Ma, X. Zeng, X. Zhan, J. Huang, *Adv. Mater.* **2017**, *29*, 1604545.
- [15] X. Zheng, B. Chen, J. Dai, Y. Fang, Y. Bai, Y. Lin, H. Wei, X. C. Zeng, J. Huang, *Nat. Energy* **2017**, *2*, 17102.
- [16] O. S. Game, G. J. Buchsbaum, Y. Zhou, N. P. Padture, A. I. Kingon, *Adv. Funct. Mater.* **2017**, *27*, 1606584.
- [17] B. Wu, K. Fu, N. Yantara, G. Xing, S. Sun, T. C. Sum, N. Mathews, *Adv. Energy Mater.* **2015**, *5*, 1500829.
- [18] D. W. deQuilettes, W. Zhang, V. M. Burlakov, D. J. Graham, T. Leijtens, A. Osherov, V. Bulovic, H. J. Snaith, D. S. Ginger, S. D. Stranks, *Nat. Commun.* **2016**, *7*, 11683.
- [19] T. Bu, X. Liu, Y. Zhou, J. Yi, X. Huang, L. Luo, J. Xiao, Z. Ku, Y. Peng, F. Huang, Y. B. Cheng, J. Zhong, *Energy Environ. Sci.* **2017**, *10*, 2509.
- [20] P. Calado, A. M. Telford, D. Bryant, X. Li, J. Nelson, B. C. O'Regan, P. R. F. Barnes, *Nat. Commun.* **2016**, *7*, 13831.
- [21] E. L. Unger, E. T. Hoke, C. D. Bailie, W. H. Nguyen, A. R. Bowring, T. Heumüller, M. G. Christoforo, M. D. McGehee, *Energy Environ. Sci.* **2014**, *7*, 3690.
- [22] C. Eames, J. M. Frost, P. R. F. Barnes, B. C. O'Regan, A. Walsh, M. S. Islam, *Nat. Commun.* **2015**, *6*, 7497.
- [23] J. Haruyama, K. Sodeyama, L. Han, Y. Tateyama, *J. Am. Chem. Soc.* **2015**, *137*, 10048.
- [24] Y. Yuan, J. Huang, *Acc. Chem. Res.* **2016**, *49*, 286.
- [25] D. A. Egger, A. M. Rappe, L. Kronik, *Acc. Chem. Res.* **2016**, *49*, 573.
- [26] T. Y. Yang, G. Gregori, N. Pellet, M. Graetzel, J. Maier, *Angew. Chem.* **2015**, *54*, 7905.
- [27] J. M. Azpiroz, E. Mosconi, J. Bisquert, F. De Angelis, *Energy Environ. Sci.* **2015**, *8*, 2118.
- [28] Y. Shao, Z. Xiao, C. Bi, Y. Yuan, J. Huang, *Nat. Commun.* **2014**, *5*, 5784.
- [29] D. Wei, J. Ji, D. Song, M. Li, P. Cui, Y. Li, J. M. Mbengue, W. Zhou, Z. Ning, N. G. Park, *J. Mater. Chem. A* **2017**, *5*, 1406.
- [30] W. Ke, C. Xiao, C. Wang, B. Saparov, H. S. Duan, D. Zhao, Z. Xiao, P. Schulz, P. Harvey, W. Liao, W. Meng, Y. Yu, A. J. Cimaroli, C. S. Jiang, K. Zhu, M. Al-Jassim, G. Fang, D. B. Mitzi, Y. Yan, *Adv. Mater.* **2016**, *28*, 5214.
- [31] Y. Liu, K. Palotas, X. Yuan, T. Hou, H. Lin, Y. Li, S. T. Lee, *ACS Nano* **2017**, *11*, 2060.
- [32] Q. Wang, B. Chen, Y. Liu, Y. Deng, Y. Bai, Q. Dong, J. Huang, *Energy Environ. Sci.* **2017**, *10*, 516.
- [33] N. Klein-Kedem, D. Cahen, C. Hodes, *Acc. Chem. Res.* **2016**, *49*, 347.
- [34] Z. Xiao, Y. Yuan, Y. Shao, Q. Wang, Q. Dong, C. Bi, P. Sharma, A. Gruverman, J. Huang, *Nat. Mater.* **2015**, *14*, 193.
- [35] R. Dong, Y. Fang, J. Chae, J. Dai, Z. Xiao, Q. Dong, Y. Yuan, A. Centrone, X. C. Zeng, J. Huang, *Adv. Mater.* **2015**, *27*, 1912.

- [36] J. T. Davis, G. P. Spada, *Chem. Soc. Rev.* **2007**, 36, 296.
- [37] J. W. Steed, *Nat. Chem.* **2011**, 3, 9.
- [38] S. Grimme, *WIREs Comput. Mol. Sci.* **2011**, 1, 211.
- [39] J. Y. Lee, S. J. Lee, H. S. Choi, S. J. Cho, K. S. Kim, T. K. Ha, *Chem. Phys. Lett.* **1995**, 232, 67.
- [40] K. S. Kim, J. Y. Lee, S. J. Lee, T. K. Ha, D. H. Kim, *J. Am. Chem. Soc.* **1994**, 116, 7399.
- [41] M. S. Marshall, R. P. Steele, K. S. Thanthiriwatte, C. D. Sherrill, *J. Phys. Chem. A* **2009**, 113, 13628.
- [42] I. Soteras, M. Orozco, F. J. Luque, *Phys. Chem. Chem. Phys.* **2008**, 10, 2616.
- [43] J. Padchasri, R. Yimnirun, *J. Alloys Compd.* **2017**, 720, 63.
- [44] L. Liu, J. A. Mcleod, R. Wang, P. Shen, S. Duhm, *Appl. Phys. Lett.* **2015**, 107, 061904.
- [45] W. Huang, S. Sadhu, S. Ptasinska, *Chem. Mater.* **2017**, 29, 8478.
- [46] W. J. Yin, T. Shi, Y. Yan, *Appl. Phys. Lett.* **2014**, 104, 063903.
- [47] H. Shi, M. H. Du, *Phys. Rev. B* **2014**, 90, 174103.
- [48] Z. Xiao, W. Meng, J. Wang, Y. Yan, *ChemSusChem* **2016**, 9, 2628.
- [49] S. Cong, H. Yang, Y. Lou, L. Han, Q. Yi, H. Wang, Y. Sun, G. Zou, *ACS Appl. Mater. Interfaces* **2017**, 9, 2295.
- [50] D. Song, P. Cui, T. Wang, D. Wei, M. Li, F. Cao, X. Yue, P. Fu, Y. Li, Y. He, B. Jiang, M. Trevor, *J. Phys. Chem. C* **2015**, 119, 22812.
- [51] Y. Zhao, J. Wei, H. Li, Y. Yan, W. Zhou, D. Yu, Q. Zhao, *Nat. Commun.* **2016**, 7, 10228.
- [52] W. Xie, K. A. McGarry, F. Liu, Y. Wu, P. P. Ruden, C. J. Douglas, C. D. Frisbie, *J. Phys. Chem. C* **2013**, 117, 11522.
- [53] C. Liu, K. Huang, W. T. Park, M. Li, T. Yang, X. Liu, L. Liang, T. Minari, Y. Y. Noh, *Mater. Horiz.* **2017**, 4, 608.
- [54] V. Nandal, P. R. Nair, *ACS Nano* **2017**, 11, 11505.
- [55] M. Bag, L. A. Renna, R. Y. Adhikari, S. Karak, F. Liu, P. M. Lahti, T. P. Russell, M. T. Tuominen, D. Venkataraman, *J. Am. Chem. Soc.* **2015**, 137, 13130.
- [56] W. Li, H. Dong, X. Guo, N. Li, J. Li, G. Niu, L. Wang, *J. Mater. Chem. A* **2014**, 2, 20105.
- [57] A. Dualeh, N. Tetreault, T. Moehl, P. Gao, M. K. Nazeeruddin, M. Gratzel, *Adv. Funct. Mater.* **2014**, 24, 3250.
- [58] Q. Lin, A. Armin, R. Chandra, R. Nagiri, P. L. Burn, P. Meredith, *Nat. Photonics* **2015**, 9, 106.
- [59] J. P. Correa-Baena, M. Anaya, G. Lozano, W. Tress, K. Domanski, M. Saliba, T. Matsui, T. J. Jacobsson, M. E. Calvo, A. Abate, M. Gratzel, H. Miguez, A. Hagfeldt, *Adv. Mater.* **2016**, 28, 5031.
- [60] Q. Jiang, L. Zhang, H. Wang, X. Yang, J. Meng, H. Liu, Z. Yin, J. Wu, X. Zhang, J. You, *Nat. Energy* **2017**, 2, 16177.
- [61] D. Song, D. Wei, P. Cui, M. Li, Z. Duan, T. Wang, J. Ji, Y. Li, J. M. Mbengue, Y. Li, Y. He, M. Trevor, N. G. Park, *J. Mater. Chem. A* **2016**, 4, 6091.
- [62] P. Cui, D. Wei, J. Ji, D. Song, Y. Li, X. Lin, J. Huang, T. Wang, J. You, M. Li, *Solar RRL* **2017**, 1, 1600027.